Supplementary Information

An efficient bi-functional Ir based catalyst for acidic overall water splitting reaction

Chunyan Wang[a], Fulin Yang[a], Ligang Feng*[a]

[a]School of Chemistry and Chemical Engineering, Yangzhou University, Yangzhou 225002, P.R China.

E-mail: ligang.feng@yzu.edu.cn, fenglg11@gmail.com

Experimental sections

Chemicals and materials

Chemicals

All the reagents in the experiment were analytical grade and used as received. Sodium tellurate (Na$_2$TeO$_3$), Iridium chloride hydrate (IrCl$_3 \cdot x$H$_2$O, Mw=298.58), ethylene glycol (C$_2$H$_6$O$_2$, EG), polyvinylpyrrolidone (Mw=58000) (PVP) and L-ascorbic acid were purchased from Shanghai Aladdin Bio-Chem Technology Co., Ltd. Sulphuric acid (H$_2$SO$_4$) were purchased from Sinopharm Chemical Reagent Co., Ltd. Nafion (5 wt%) was purchased from Sigma-Aldrich. Commercial Pt/C (20 wt% Pt) catalyst was bought from Alfa Aesar (Tianjin) Chemical Co., Ltd. All solutions were prepared with ultrapure water (Thermo Fisher Scientific (USA) Co., Ltd).

Preparation of Ir/Te nanorods

The synthesis of Ir/Te nanorods consisted of two steps:

(1) Preparation of Te nanorods

In the first step, 230 mg Na$_2$TeO$_3$, 450 mg L-ascorbic acid, and 100 mg PVP were added into a beaker and dispersed in 30 mL of EG under vigorous magnetic stirring at room temperature to form a homogeneous solution. The obtained solution was transferred into the Teflon-lined stainless steel with a volume capacity of 50 mL, sealed, and reacted at 150 °C for 6 h. Finally, the Te nanorods were precipitated using acetone cleaned with ultrapure water, and dried overnight in a vacuum at 60 °C.

(2) Preparation of Ir/Te nanorods

In the report[1], a template-assisted synthesis method was reported to fabricate 1D porous Ir-Te nanowires (Ir-Te NWs) by using Te NWs serving as the template; specifically, the Ir(acac)$_3$ was used as the precursor of noble metal Ir, and the hydrothermal temperature and time were 200 °C and 9.5 h, respectively. in order to get the catalyst of a thin Ir nanoparticles layer over the surface of Te nanorods, the modified hydrothermal method was employed by reducing the fabrication time and temperature. Specifically, in the second step, 50 mg Te nanorods obtained above were ultrasonically dispersed in 45 mL EG to form a uniform suspension. Under stirring, 20 mg IrCl$_3 \cdot x$H$_2$O (containing 12.8 mg Ir metal) was added to the suspension. The obtained solution was transferred into the

Teflon-lined stainless steel with a volume capacity of 50 mL, sealed, and reacted at 160 °C for 6 h. At last, the suspension was filtered, washed, and dried overnight at 60 °C in a vacuum to obtain Ir/Te nanorods catalyst. The nominal atomic percentage of Ir in the Ir/Te catalyst was calculated to be 6.7%. Herein, the Te nanorods were serviced as the supporting substrate for the Ir nanoparticles anchoring, which was different from the reports that Te functionalized as a sacrifice template for the galvanic replacement to generate porous and mixed Ir-Te composite [1,2]. This kind of catalyst was more suited for the metal-support interaction analysis.

Physical characterization

Powder X-ray diffraction (XRD) patterns were tested on a Bruker D8 Advance powder X-ray diffractometer using a Cu K$_\alpha$ (λ=1.5405 Å) radiation source operating at 40 kV and 40 mA and at a scanning rate of 5°min^{-1}. The morphology and microstructure were analyzed by Field Emission Scanning Electron Microscope (FESEM, Hitachi, S-4800 II, Japan). All transmission electron microscopy (TEM) and high-resolution TEM (HRTEM) measurements were conducted on a TECNAI G2 operating at 300 kV. The energy-dispersive X-ray detector spectrum (EDX) images were obtained on a TECNAI G2 transmission electron microscope equipped with an EDXA detector. All X-Ray photoelectron spectroscopy (XPS) measurements were carried out on Kratos XSAM-800 spectrometers with an Al K$_\alpha$ radiation source. The accurate element content was determined by the iCAPTM QC inductively coupled plasma mass spectrometry (ICP-MS).

Electrochemical Pre-treatment

All the electrochemical measurements are carried out with a Bio-Logic VSP electrochemical workstation (Bio-Logic Co., France) and a conventional three-electrode system. The working electrode is a glassy carbon electrode (3 mm diameter, 0.07 cm^2). The graphite rod and the saturated calomel electrode (SCE, Hg/Hg$_2$Cl$_2$) serve as a counter and a reference electrode through a double salt bridge and lugging capillary tip, the potential was carefully checked before and after the relevant measurements. The potentials reported in the work were converted to the reversible hydrogen electrode (RHE), E(RHE) = E(SCE) + 0.0591*pH + 0.242 V. The equation of η(V) = E(RHE) - E$^\theta$ was used to calculate the overpotential of these electrocatalysts, where E$^\theta$ represents the thermodynamic potential for OER (1.23 V *vs*. RHE). The catalyst ink was prepared by ultrasonically

dispersing a mixture containing 2 mg of catalyst and 0.5 mg carbon black, 475 μL of ethanol, and 25 μL of a 5 wt% Nafion solution. Next, pipette 10 μL of the catalyst ink onto a pre-cleaned working electrode, and then clamp the electrode with the electrode clip to start the test.

Electrochemical measurements

For HER, OER, and overall-water-splitting measurement, the linear sweep voltammograms (LSV) of all catalysts were recorded at a scan rate of 5 mV s^{-1} in 0.5 M H$_2$SO$_4$ solution. The current density was obtained by normalizing the current to the geometric surface.

The overall water splitting was carried out in a two-electrode system using Ir/Te NRs catalyst both as the anode and cathode, and the polarization curve was recorded at a scan rate of 5 mV s^{-1} in 0.5 M H$_2$SO$_4$ solution with the potential range from 1.0 V to 1.8 V. No iR-compensation was applied to the overall water splitting measurement. The long-term durability tests were conducted at 1.56 V and to drive 10 mA cm^{-2} in 0.5 M H$_2$SO$_4$ solution.

Tafel slope analysis

The overpotential values are defined by the Tafel equation: $\eta = a + b\log|j|$, where η (V) is the overpotential, j (mA cm^{-2}) is the current density; b (mV dec^{-1}) represents the Tafel slope.

Electrochemical Impedance Spectroscopy (EIS) analysis

The ohmic resistance used for iR-compensation was obtained from electrochemical impedance spectroscopy measurements with frequencies ranging from 1000 kHz to 10 mHz with an amplitude of 5 mV.

ECSA measurements and calculation

The electrochemical surface area (ECSA) was evaluated in terms of double layer capacitance (C_{dl}). The ECSA was estimated by cyclic voltammetry (CV) without Faradaic processes occurred region from 0.242 to 0.342 V *vs*. RHE in 0.5 M H$_2$SO$_4$ at scan rates of 20, 40, 60, 80, and 100 mV s^{-1}. The C_{dl} was estimated by plotting the $\triangle J = (Ja - Jc)/2$ at 0.292 V *vs*. RHE against the scan rate. The linear slope is the double layer capacitance C_{dl}. The specific capacitance is evaluated for a flat surface by assuming 40 μF cm^{-2} according to previous literature. The electrochemically active surface area was achieved by normalizing the double-layer capacitance to a standard specific capacitance. The roughness factor (R_f) can be calculated by (ECSA) based on the geometric surface area of the electrode (0.07 cm^2).

Specific activity and Turnover frequency (TOF)

The specific activity was obtained by normalizing the apparent current to ECSA. The TOF (s^{-1}) for OER analysis, the TOF can be calculated with the following equation TOF = I/(4*F*n). Where I is the current (A) during linear sweep measurement, F is the Faraday's constant (96500 C/mol), and n is the number of active sites (mol). The factor 1/4 is based on the consideration that four electrons are required to produce one oxygen molecule. Herein, all the Ir metal atoms on the electrode are assumed to be the active sites. And the amount of the Ir in the electrode is known and the molar amount of the Ir can be calculated according to the formula: n (mol) = catalyst loading on the glassy carbon electrode*metal content/molar mass of metal.

Stability test and Chronoamperometry (CA) measurements

The dynamical stability was tested for 1000 cycles at the constant scan rate of 50 mV s^{-1}. After 1000 cycles, the polarization curve was recorded for comparison with the initial curve. To estimate the stability of the catalysts, the chronoamperometry (CA) was performed at a potential of -0.04V *vs*. RHE for HER and potential of 1.52 V *vs*. RHE in 0.5 M H_2SO_4 solution.

Computational methods

The CASTEP module of the Materials Studio software (Accelrys Inc.) was employed for the quantum chemistry calculations. Perdew−Burke−Ernzerh (PBE) of approximation was selected as the generalized gradient approximation (GGA) method to calculate the exchange-correlation energy. The Broyden−Fletcher−Goldfarb−Shanno (BFGS) scheme was selected as the minimization algorithm. The energy cut off is 380 eV and the SCF tolerance is $1.0×10^{-6}$ eV/atom. The optimization is completed when the energy, maximum force, maximum stress and maximum displacement are smaller than $5.0×10^{-6}$ eV/atom, 0.01 eV/Å, 0.02 GPa and $5.0×10^{-4}$ Å, respectively. A vacuum slab exceeding 15 Å was employed in the z direction to avoid the interaction between two periodic units. The adsorption energy (E_{ads}) between the surface and adsorbed particles was computed by eqs (1).

$$E_{ads} = E_{molecule+surface} - E_{molecule} - E_{surface} 。 \qquad (1)$$

where $E_{molecule+surface}$ is the total energy of the system after adsorbing the molecule, $E_{molecule}$ is the energy of adsorption molecules, and $E_{surface}$ is the total energy of the system before adsorbing the molecule.

The Gibbs free energy of the reaction and Gibbs free energy of adsorption of the hydrogen atom can be obtained from eqs (2) and eqs (3).

$$\Delta E_{H*} = E_{surface + H*} - E_{surface} - 1/2\, E_{H2} \qquad (2)$$

$$\Delta G_{H*} = \Delta E_H + \Delta E_{ZEP} - T\Delta S_H \qquad (3)$$

where the $E_{surface + H}$ represents the total energy of the system after adsorbing the H molecule, $E_{surface}$ represents the total energy of the system before adsorbing the H molecule, and E_{H2} represents the total energy of a gas phase H_2 molecule.

In addition, it should be noted that the DFT calculation of supported catalysts is mainly devoted to the study of the intrinsic activity of the catalyst and its mechanism of action in the catalytic reaction, without consideration of the atomic ratio of the constructed catalyst. When calculating the Gibbs free energy, we mainly explored the intrinsic activity of a single active site in different catalysts to avoid the influence of noble metal content on the results.
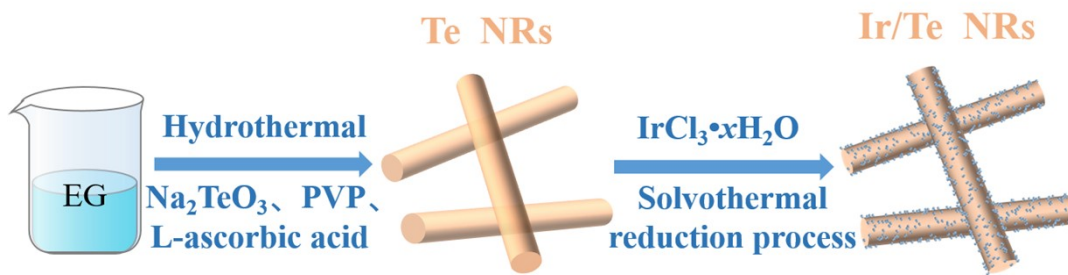
Figure S1. Schematic the synthetic route of Te NRs and Ir/Te NRs.
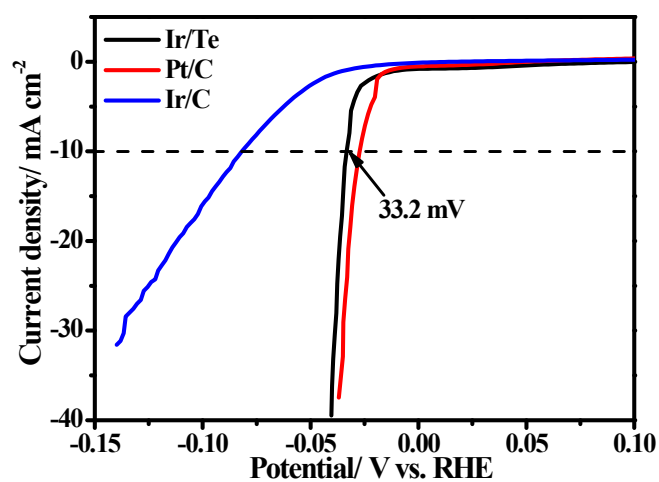
Figure S2. HER polarization curves of Ir/Te, Pt/C, and Ir/C in N_2-saturated 0.5 M H_2SO_4 solution at a scan rate of 5 mV s^{-1} with iR-correction.
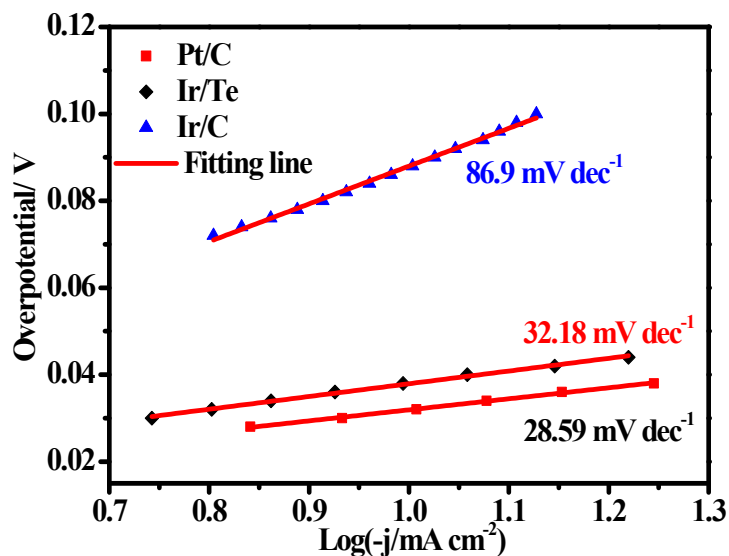
Figure S3. Tafel plots of the Ir/Te NRs, Pt/C, and Ir/C catalyst for HER.
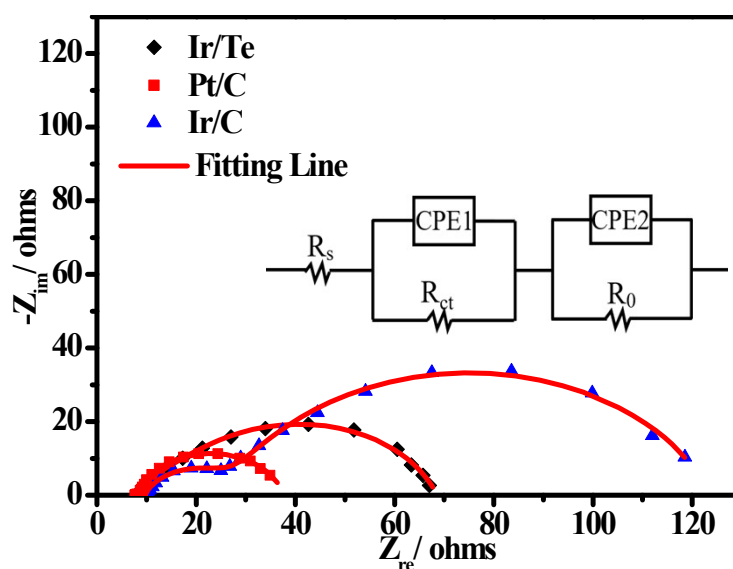
Figure S4. Nyquist plots of the Ir/Te NRs, Pt/C, and Ir/C catalyst for HER and the equivalent circuit diagram used for EIS data fitting in the HER, where R_s is a sign of the uncompensated solution resistance, R_{ct} is a charge transfer resistance arising from the relevant electrochemical oxidation, R_0 is associated with the contact resistance between the catalyst and the glassy carbon electrode, and the CPE is regarded as the double layer capacitor from the catalyst/support and catalyst solution.
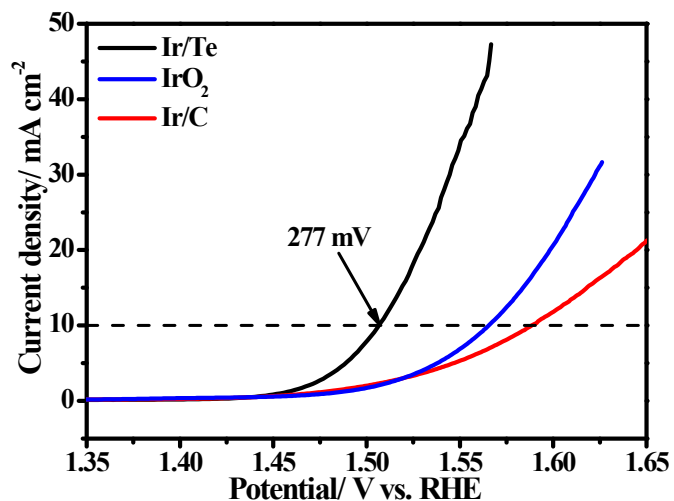
Figure S5. OER polarization curves of Ir/Te, IrO_2, and Ir/C in N_2-saturated 0.5 M H_2SO_4 solution at a scan rate of 5 mV·s^{-1} with iR correction.
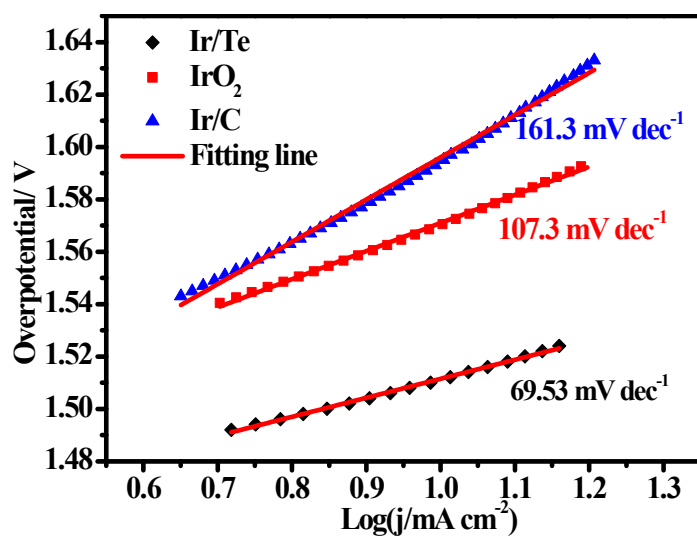
Figure S6. Tafel plots of the Ir/Te NRs, IrO_2, and Ir/C catalyst for OER.
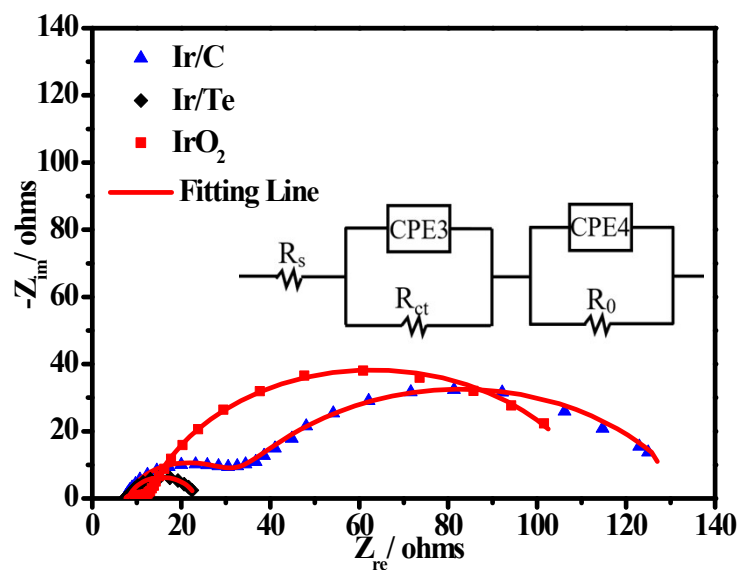
Figure S7. Nyquist plots of the Ir/Te NRs, IrO$_2$, and Ir/C catalyst for OER. and the equivalent circuit diagram used for EIS data fitting in the OER, where the physical meaning of electrical components is similar to that for HER.
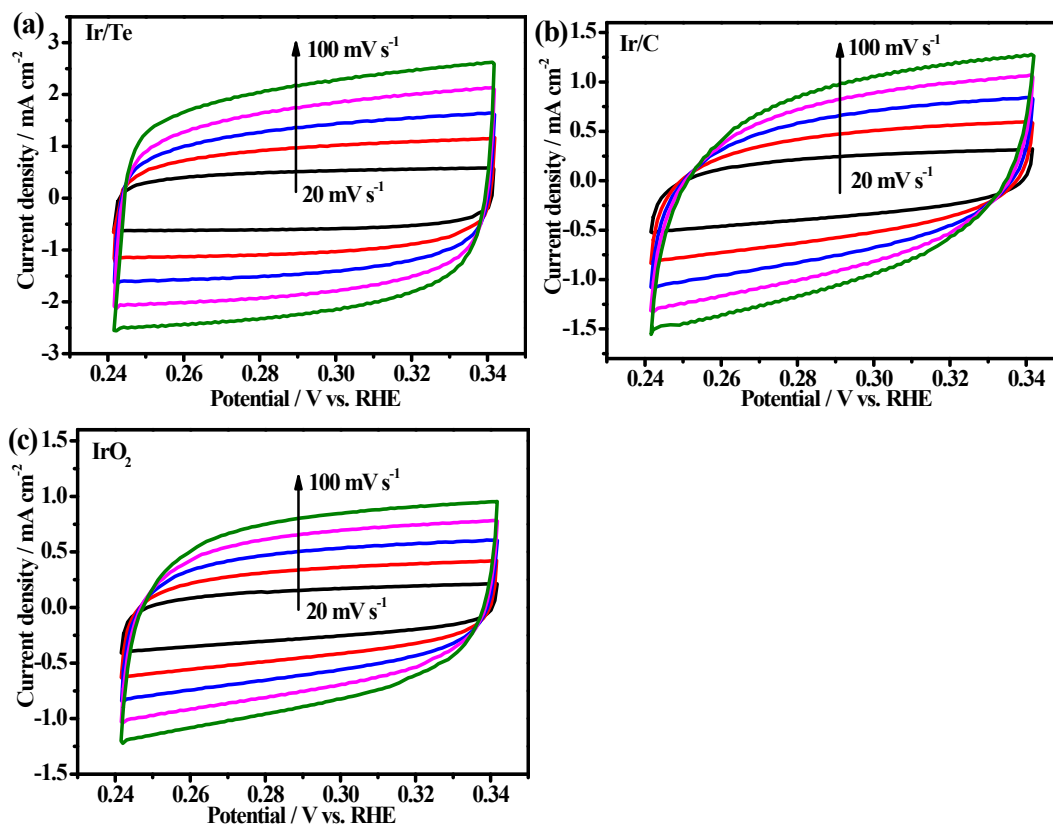
Figure S8. Cyclic voltammograms for the double layer capacitance from 0.242 V to 0.342 V for Ir/Te NRs, Ir/C, and IrO$_2$.
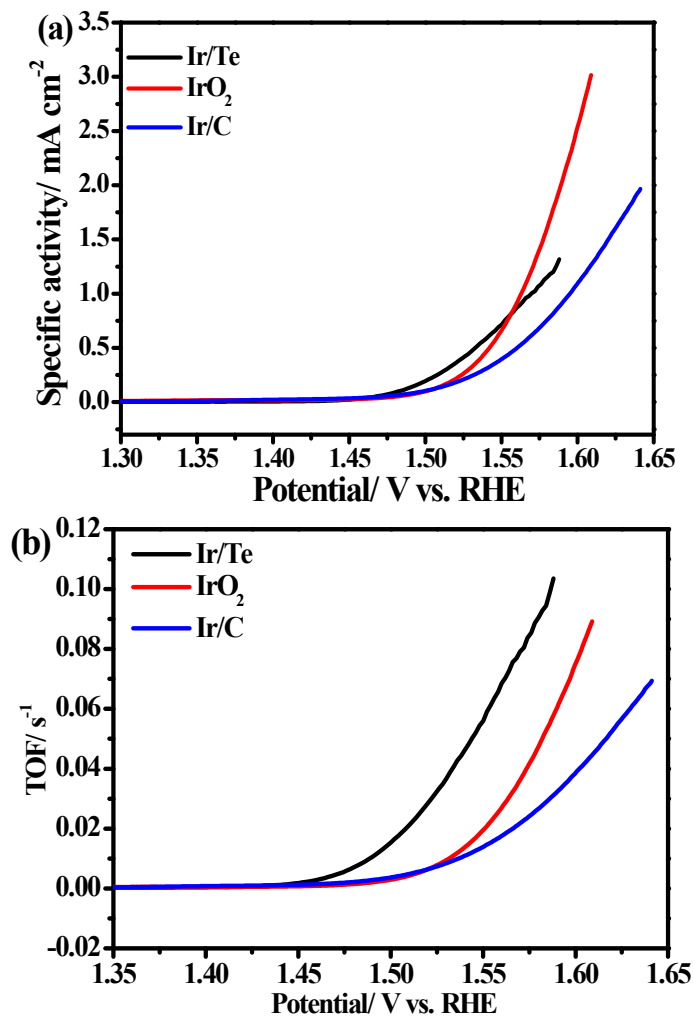
Figure S9. (a) Specific activity and (b) TOF of Ir/Te NRs, Ir/C, and IrO$_2$ for OER
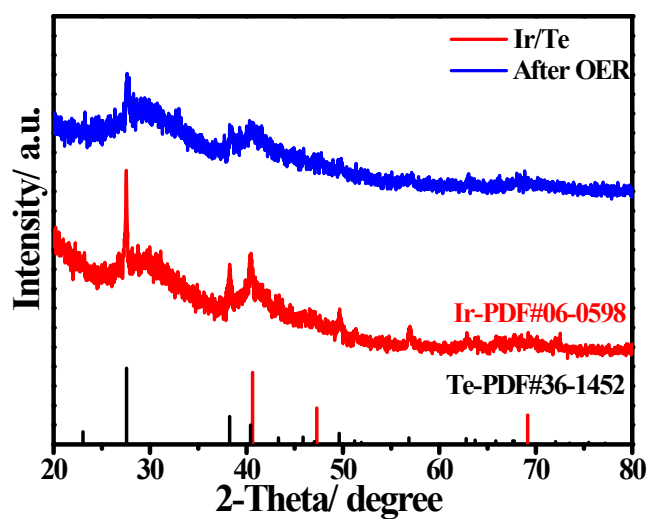
Figure S10. XRD patterns of Ir/Te NRs before and after the 20 h CA stability test of OER.

11
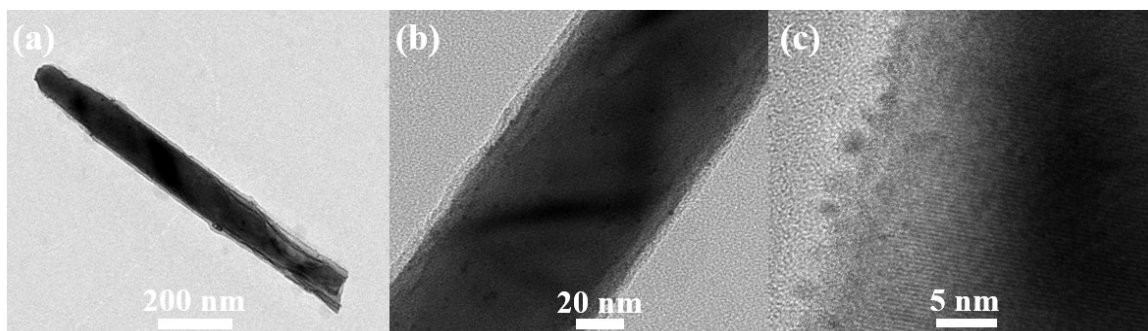
Figure S11. (a) TEM image; (b-c) High-resolution TEM image for Ir/Te NRs after 20 h OER long-term stability test.
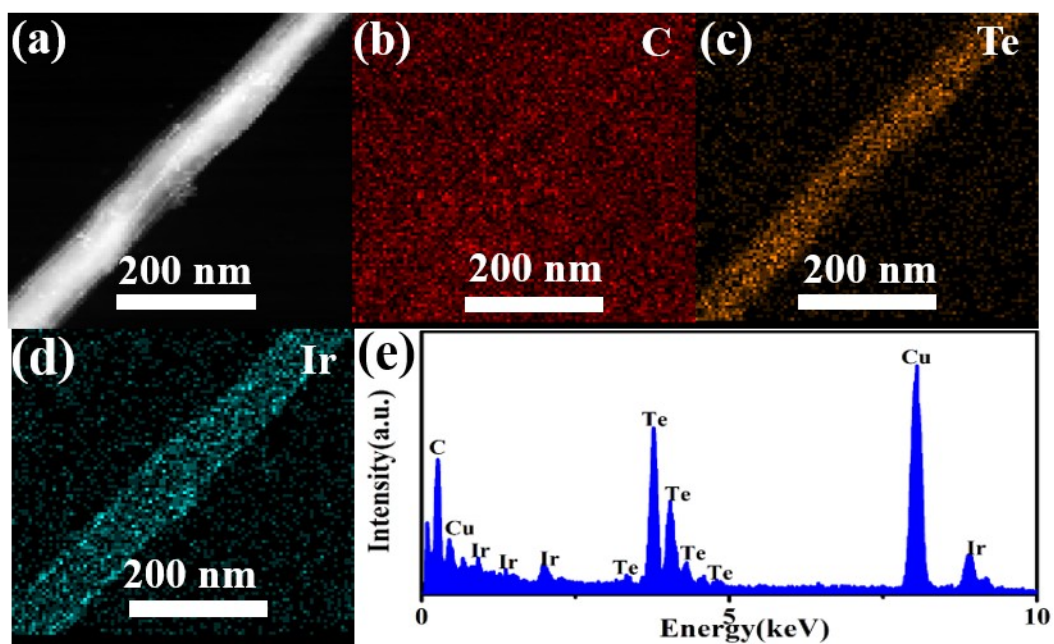
Figure S12. (a-d) Corresponding elemental mappings and overlap image of element mapping images; (e) EDX image of Ir/Te NRs after OER.
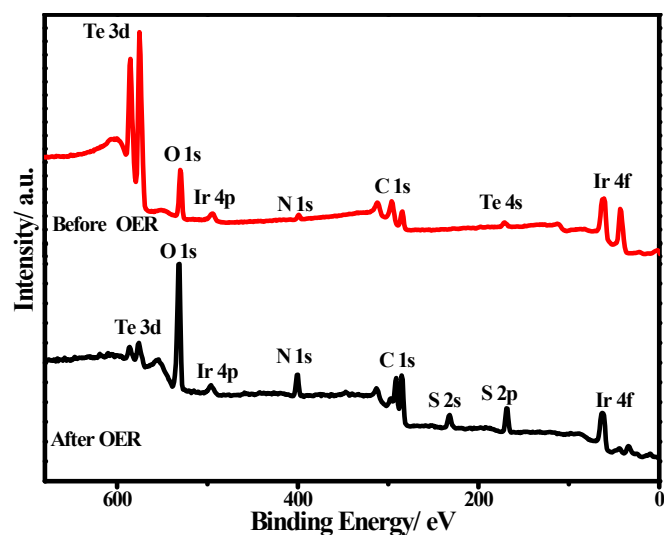
Figure S13. The high-resolution XPS survey spectra before and after 20 h OER long-term stability test of Ir/Te NRs.
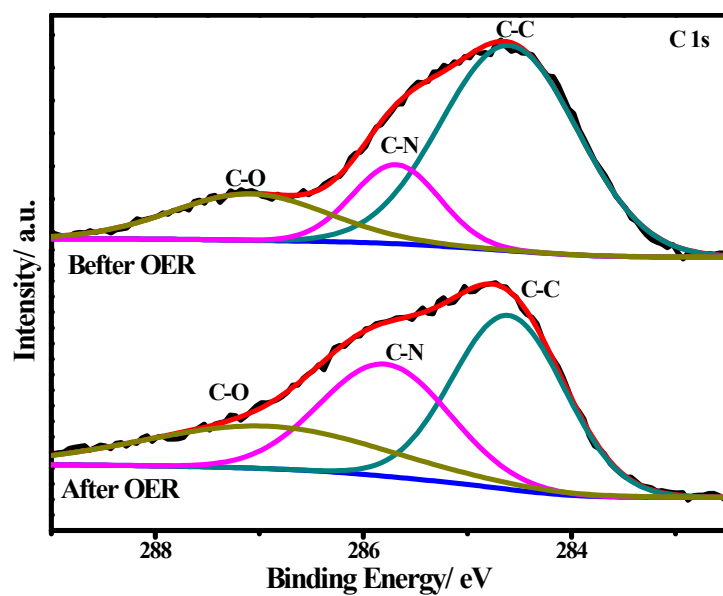
Figure S14. The high-resolution XPS spectra of the C 1s before and after OER of Ir/Te NRs.
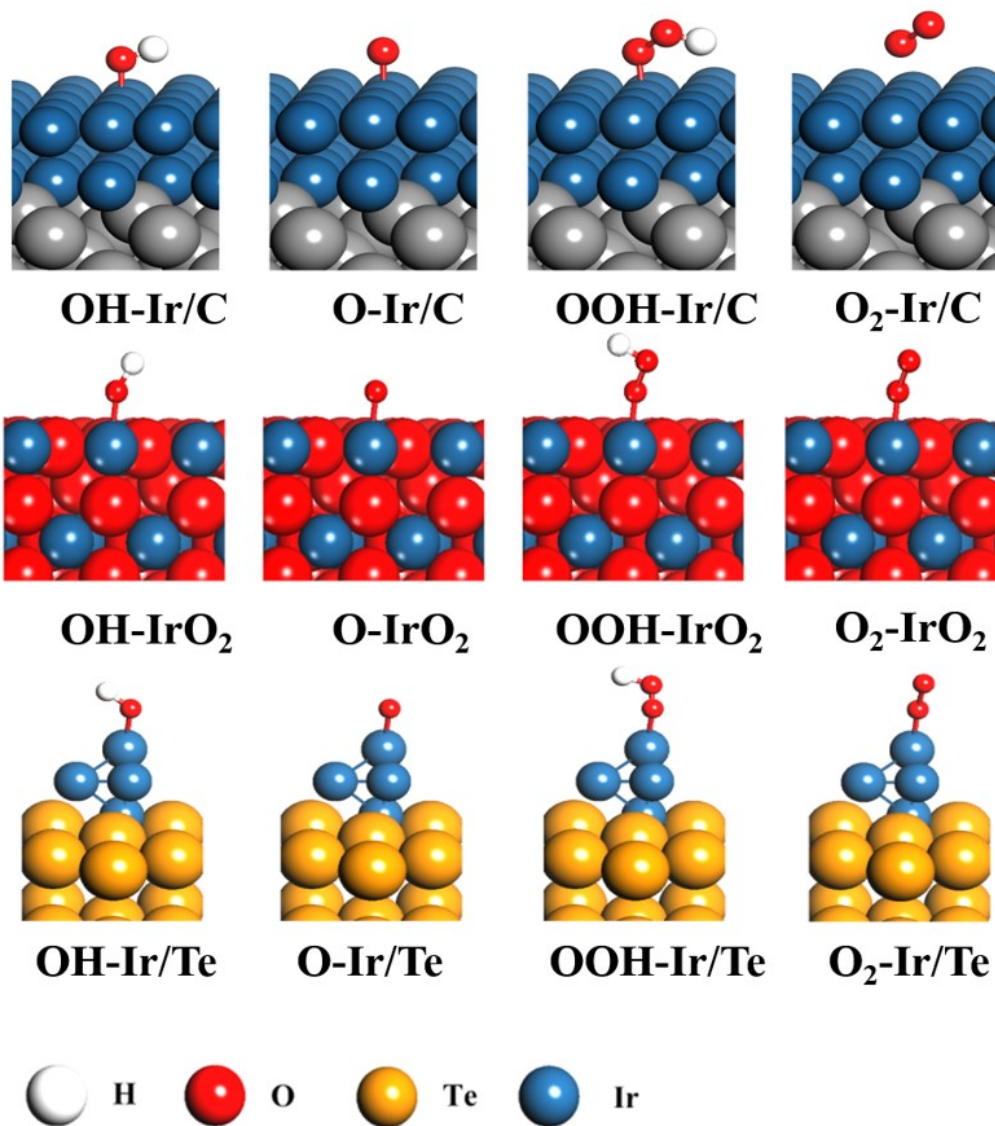
Figure S15. In the OER process, the model of Ir/C, IrO_2, and Ir/Te adsorption at each step.
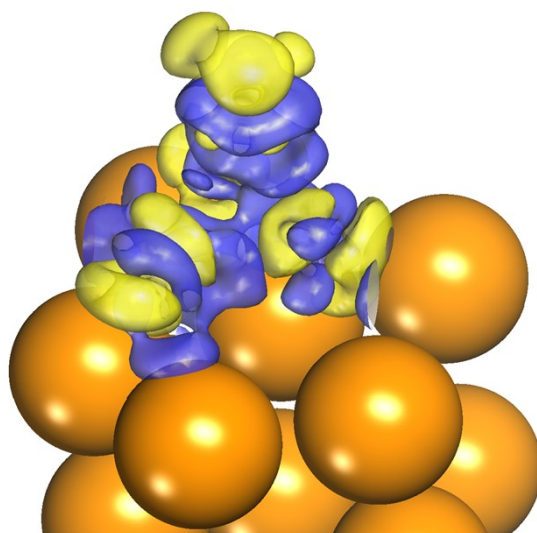
Figure S16. The differential charge density plot of Ir/Te. The blue and yellow regions represent electron accumulation and depletion, respectively.
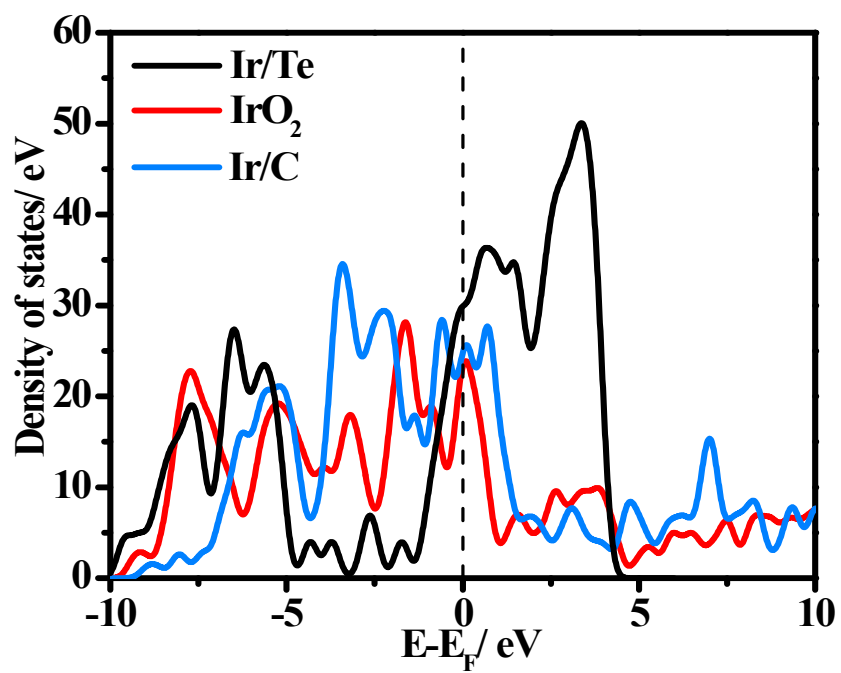
Figure S17. The density of states of IrO_2, Ir/C, and Ir/Te.

Table S1. The elemental content of Ir/Te NRs catalyst was analyzed by EDS, XPS, and ICP-MS.

Element	Atomic ratio % (EDS)	Atomic ratio % (XPS)	Atomic ratio % (ICP-MS)
Te	93.02	91.72	93.27
Ir	6.98	8.28	6.73

Table S2. EIS fitting parameters for different catalyst samples for HER in 0.5 M H_2SO_4 solution.

Sample	R_s/ Ω	R_{ct}/ Ω	CPE1/ S S^{-n}	R_0/ Ω	CPE2/ S S^{-n}	Chi squared
Ir/Te NRs	8.36	46.45	8.04E-04	12.98	7.04E-04	1.902E-04
Pt/C	7.65	29.33	3.26E-04	6.97	4.38E-03	1.789E-04
Ir/C	9.67	114.5	1.39E-04	23.6	2.31E-04	2.219E-04

Table S3. EIS fitting parameters for different catalyst samples for OER in 0.5 M H_2SO_4 solution.

Sample	R_s/ Ω	R_{ct}/ Ω	CPE3/ S S^{-n}	R_0/ Ω	CPE4/ S S^{-n}	Chi squared
Ir/Te NRs	7.55	15.74	1.09E-03	2.2	8.79E-04	1.588E-04
IrO_2	8.013	104.1	1.96E-05	30.65	8.66 E-04	6.724E-04
Ir/C	9.76	127.2	4.72E-05	3.18	6.51E-04	1.057E-03

Table S4. The C_{dl}, ECSA, R_f values and specific activity and TOF values at 1.51 V *vs*. RHE of Ir/Te NRs and their comparison samples.

Sample	C_{dl}/ mF cm^{-2}	ECSA/ cm^2	R_f	Specific activity/ mA cm^{-2}	TOF/ S^{-1}
Ir/Te NRs	20.5	35.9	512.5	0.27	0.021
IrO$_2$	7.7	13.5	192.5	0.145	0.0043
Ir/C	9.2	16.1	230	0.137	0.0048

Table S5. The binding energy of the Ir $4f_{7/2}$ and Ir $4f_{5/2}$ components for the Ir/Te NRs and the Ir/Te NRs catalysts after 20 h OER long-term stability test.

Catalysts	Ir $4f_{7/2}$		Ir $4f_{5/2}$		Content	Ir(0)/ Ir(+4)
	Peak	Binding energy / eV	Peak	Binding energy / eV		
Ir/Te NRs	Ir (0)	60.6	Ir (0)	63.6	56.7 %	1.31
	Ir (+4)	61.6	Ir (+4)	64.6	43.29 %	
Ir/Te NRs after OER	Ir (0)	61	Ir (0)	64	47.36 %	0.9
	Ir (+4)	62	Ir (+4)	65	52.63 %	

Table S6. The binding energy of the Te $3d_{5/2}$ and Te $3d_{3/2}$ components for the Ir/Te NRs and the Ir/Te NRs catalysts after 20 h OER long-term stability test.

Catalysts	Te $3d_{5/2}$		Te $3d_{3/2}$		Content	Te(0)/Te(+4)
	Peak	Binding energy / eV	Peak	Binding energy / eV		
Ir/Te NRs	Te(0)	573.1	Te(0)	583.5	38.78 %	0.63
	Te(+4)	576.1	Te(+4)	586.5	61.21%	
Ir/Te NRs after OER	Te(0)	573.8	Te(0)	584.2	21.65 %	0.27
	Te(+4)	576.8	Te(+4)	587.2	78.34 %	

Table S7. The Mulliken charge of Ir atoms in Ir/Te NRs catalyst. The positive/negative value corresponds to loss/gain of the electron.[3]

Number	Ir atoms cluster	Mulliken charge/ e
1	Ir	-0.28
2	Ir	-0.24
3	Ir	0.02
4	Ir	-0.21
Total Mulliken charge of Ir / e		-0.71

Table S8. Comparison of electrocatalytic performance of Ir/Te NRs with recently reported noble metal based electrocatalysts for HER in acidic media.

Catalysts	Electrolyte	Current density	Overpotential/ mV	Ref.
Ir/Te NRs	0.5 M H_2SO_4	10 mA cm^{-2}	38.2	This work
$Pd_{0.5}@Ir_{0.5}$/CNT	0.5 M H_2SO_4	10 mA cm^{-2}	35	[4]
$Ru@V-RuO_2$/C HMS	0.5 M H_2SO_4	10 mA cm^{-2}	46	[5]
La-doped RuO_2	0.5 M H_2SO_4	10 mA cm^{-2}	71	[6]
Ru-g-CN	0.5 M H_2SO_4	10 mA cm^{-2}	54.5	[7]
Ru−KB−H−6H	0.5 M H_2SO_4	10 mA cm^{-2}	52	[8]
$Ru@LCO_{2.5}$	0.5 M H_2SO_4	10 mA cm^{-2}	150	[9]
$Ru@Ti_3C_2T_x$-NS	0.5 M H_2SO_4	10 mA cm^{-2}	46.75	[10]
B-Ru@CNT	0.5 M H_2SO_4	10 mA cm^{-2}	62	[11]
$Ru-MoSe_2$/CMT	0.5 M H_2SO_4	10 mA cm^{-2}	109	[12]
Ru_{1+NPs}/N–C	0.5 M H_2SO_4	10 mA cm^{-2}	75	[13]
$Ru-SA/Ti_3C_2T_x$	0.1 M $HClO_4$	10 mA cm^{-2}	70	[14]

Table S9. Comparison of electrocatalytic performance of Ir/Te NRs with recently reported noble metal based electrocatalysts for OER in acidic media.

Catalysts	Electrolyte	Current density	Overpotential/ mV	Ref.
Ir/Te NRs	0.5 M H_2SO_4	10 mA cm^{-2}	281	This work
Ir@N-G-600	0.5 M H_2SO_4	10 mA cm^{-2}	314.6	[15]
Pt-Ir-Pd nanocage	0.5 M H_2SO_4	10 mA cm^{-2}	372	[16]
P-IrO$_x$@DG	0.5 M H_2SO_4	10 mA cm^{-2}	365	[17]
Ir-CeO$_2$-C	0.1 M $HClO_4$	10 mA cm^{-2}	283	[18]
IrO$_x$/Lu$_{1.25}$Ir$_1$O$_x$OH$_y$	0.1 M $HClO_4$	10 mA cm^{-2}	293	[19]
IrCo@NCNT/PC	0.5 M H_2SO_4	10 mA cm^{-2}	291	[20]
SrCo$_{0.9}$Ir$_{0.1}$O$_{3-\delta}$	0.1 M $HClO_4$	10 mA cm^{-2}	340	[21]
Ir-Te NWs	0.5 M H_2SO_4	10 mA cm^{-2}	284	[1]
IrCr	0.5 M H_2SO_4	10 mA cm^{-2}	395	[22]
Ba$_2$NdIrO$_6$	0.5 M H_2SO_4	10 mA cm^{-2}	380	[23]
IrO$_x$-network	0.5 M H_2SO_4	10 mA cm^{-2}	330	[24]
Ir$_3$CeO$_x$ /C	0.5 M H_2SO_4	10 mA cm^{-2}	299	[25]

Table S10. Comparison of electrocatalytic performance of Ir/Te NRs with recently reported noble metal based bi-functional electrocatalysts for overall-water-splitting in acidic media.

Catalysts	Electrolyte	Water splitting current density	Cell voltage/V	Ref.
Ir/Te NRs	0.5 M H_2SO_4	10 mA cm^{-2}	1.56	This work
La-doped RuO_2	0.5 M H_2SO_4	10 mA cm^{-2}	1.53	[6]
Ir@N-G-600	0.5 M H_2SO_4	10 mA cm^{-2}	1.6	[15]
IrO_x-500	0.5 M H_2SO_4	10 mA cm^{-2}	1.554	[26]
Ir-doped WO_3	0.5 M H_2SO_4	10 mA cm^{-2}	1.56	[27]
Au@$AuIr_2$	0.5 M H2SO4	10 mA cm^{-2}	1.55	[28]
Ir_3CeO_x/C	0.5 M H_2SO_4	10 mA cm^{-2}	1.635	[25]
IrNi NFs	0.5 M H_2SO_4	10 mA cm^{-2}	1.6	[29]
RuO_2-WC NPs	0.5 M H_2SO_4	10 mA cm^{-2}	1.66	[30]
Ru-RuO_2-NC	0.5 M $HClO_4$	10 mA cm^2	1.55	[31]

Reference

[1] L. Li, P. Wang, Z. Cheng, Q. Shao, X. Huang, Nano Res., 15 (2022) 1087-1093.

[2] M. Liu, S. Liu, Q. Mao, S. Yin, Z. Wang, Y. Xu, X. Li, L. Wang, H. Wang, J. Mater. Chem. A, 10 (2022) 2021-2026.

[3] Y. Chen, X. Yan, H. Geng, X. Sheng, L. Zhang, H. Wang, J. Li, Y. Cao, X. Pan, Inorg. Chem., 60 (2021) 124-129.

[4] Y. Xie, C. Chang, F. Luo, Z. Yang, ACS Appl. Mater. Interfaces, 15 (2023) 20081-20088.

[5] Y. Li, W. Wang, M. Cheng, Y. Feng, X. Han, Q. Qian, Y. Zhu, G. Zhang, Adv. Mater., 35 (2023) 2206351.

[6] Y. Wu, R. Yao, Q. Zhao, J. Li, G. Liu, Chem. Eng. J., 439 (2022) 135699.

[7] Z. Yu, Y. Li, A. TorresPinto, A.P. LaGrow, V.M. Diaconescu, L. Simonelli, M.J. Sampaio, O. Bondarchuk, I. Amorim, A. Araujo, A.M.T. Silva, C.G. Silva, J.L. Faria, L. Liu, Appl. Catal., B, 310 (2022) 121318.

[8] X. Fan, Q. Pang, ChemElectroChem, 8 (2021) 4472-4479.

[9] A. Kuchipudi, S. Nagappan, A. Karmakar, G. Sreedhar, S. Kundu, Inorg. Chem., 61 (2022) 19407-19416.

[10] Y. Yang, Z. Yu, X. An, X. Duan, M. Chen, J. Zhang, X. Hao, A. Abudula, G. Guan, Int. J. Hydrog. Energy, 48 (2023) 9163-9171.

[11] X. Sun, W. Li, J. Chen, X. Yang, B. Wu, Z. Wang, B. Li, H. Zhang, J. Colloid Interf. Sci., 616 (2022) 338-346.

[12] Y. Xue, Y. Xu, Q. Yan, K. Zhu, K. Ye, J. Yan, Q. Wang, D. Cao, G. Wang, J. Colloid Interf. Sci., 617 (2022) 594-603.

[13] S. Wang, M. Wang, Z. Liu, S. Liu, Y. Chen, M. Li, H. Zhang, Q. Wu, J. Guo, X. Feng, Z. Chen, Y. Pan, ACS Appl. Mater. Interfaces, 14 (2022) 15250-15258.

[14] X. Peng, S. Zhao, Y. Mi, L. Han, X. Liu, D. Qi, J. Sun, Y. Liu, H. Bao, L. Zhuo, H.L. Xin, J. Luo, X. Sun, Small, 16 (2020) 2002888.

[15] L. Yi, B. Feng, N. Chen, W. Li, J. Li, C. Fang, Y. Yao, W. Hu, Chem. Eng. J., 415 (2021) 129034.

[16] J. Zhu, M. Xie, Z. Chen, Z. Lyu, M. Chi, W. Jin, Y. Xia, Adv. Energy Mater., 10 (2020) 1904114.

[17] L. Zhuang, F. Xu, K. Wang, J. Li, C. Liang, W. Zhou, Z. Xu, Z. Shao, Z. Zhu, Small, 17 (2021) 2100121.

[18] X. Chen, W. Liao, M. Zhong, J. Chen, S. Yan, W. Li, C. Wang, W. Chen, X. Lu, Nano Res., 16 (2023) 7724-7732.

[19] C. Ma, X. Yang, Z. Wang, W. Sun, L. Zhu, L. Cao, X. Gong, J. Yang, ACS Appl. Mater. Interfaces, 14 (2022) 28706-28715.

[20] D. Zhao, Y. Zhu, Q. Wu, W. Zhou, J. Dan, H. Zhu, W. Lei, L. Ma, L. Li, Chem. Eng. J., 430 (2022) 132825.

[21] Y. Chen, H. Li, J. Wang, Y. Du, S. Xi, Y. Sun, M. Sherburne, J.W. Ager, A.C. Fisher, Z.J. Xu, Nat. Commun., 10 (2019) 572.

[22] A.L. Strickler, R.A. Flores, L.A. King, J.K. Nørskov, M. Bajdich, T.F. Jaramillo, ACS Appl. Mater. Interfaces, 11 (2019) 34059-34066.

[23] C. Song, J. Lim, H. Bae, S. Chung, Energ. Environ. Sci., 13 (2020) 4178-4188.

[24] A.W. Jensen, G.W. Sievers, K.D. Jensen, J. Quinson, J.A. ArminioRavelo, V. Brüser, M. Arenz, M. EscuderoEscribano, J. Mater. Chem. A, 8 (2020) 1066-1071.

[25] X. Zhao, Y. Chang, X. He, H. Zhang, J. Jia, M. Jia, J. Rare Earths, 41 (2023) 208-214.

[26] W. Quan, Y. Hou, Y. Lin, Z. Hong, R. Yang, H. Yao, Y. Huang, Inorg. Chem., 62 (2023) 4011-4019.

[27] P. Li, X. Duan, Y. Kuang, X. Sun, Small, 17 (2021) 2102078.

[28] H. Wang, Z. Chen, D. Wu, M. Cao, F. Sun, H. Zhang, H. You, W. Zhuang, R. Cao, J. Am. Chem. Soc., 143 (2021) 4639-4645.

[29] F. Lv, W. Zhang, W. Yang, J. Feng, K. Wang, J. Zhou, P. Zhou, S. Guo, Small Methods, 4 (2020) 1900129.

[30] S. Sun, H. Jiang, Z. Chen, Q. Chen, M. Ma, L. Zhen, B. Song, C. Xu, Angew. Chem. Int. Ed., 61 (2022) e202202519.

[31] L. Ai, Y. Wang, Y. Luo, Y. Tian, S. Yang, M. Chen, J. Jiang, J. Alloys Compd., 902 (2022) 163787.